Mon. Not. R. Astron. Soc. **000**, 000–000 (0000) Printed 3 September 2020 (MN LATEX style file v2.2)

Effective temperature calibration from the InfraRed Flux Method in the Gaia system

L. Casagrande[1,2⋆], The Author2[3]
[1] *Research School of Astronomy and Astrophysics, Mount Stromlo Observatory, The Australian National University, ACT 2611, Australia*
[2] *ARC Centre of Excellence for All Sky Astrophysics in 3 Dimensions (ASTRO 3D)*
[3] *Somewhere*

Received; accepted

ABSTRACT
We implement Gaia and 2MASS photometry in the InfraRed Flux Method and apply it to stars across different evolutionary status in the GALAH DR3 survey. We derive colour-effective temperature relations that take into account the effect of metallicity and surface gravity over the range $3600 \lesssim T_{\rm eff} \lesssim 9000$ K. Comparison against solar-twins, Gaia benchmark stars and the latest interferometric measurements validates the precision and accuracy of these calibrations for spectral types later than F. We assess the impact of various sources of uncertainties and provide guidelines to use our relations.

Key words:

1 INTRODUCTION

The effective temperature ($T_{\rm eff}$) of a star is one of the most fundamental stellar parameters, and its knowledge impacts virtually every stellar property, be it derived from spectroscopy, or inferred by comparing against stellar models (e.g., Nissen & Gustafsson 2018; Choi et al. 2018).

While angular diameters measured from interferometry provide the most direct way to measure effective temperatures of stars (e.g., Code et al. 1976), they require a considerable investement of time, a careful assessment of systematic uncertainties, and they are biased towards bright targets, which are often saturared in modern photometric systems (e.g., White et al. 2013; Lachaume et al. 2019; Rains et al. 2020).

Among the many indirect methods to determine $T_{\rm eff}$ is the InfraRed Flux Method (hereafter IRFM) an almost model independent photometric technique originally devised to obtain angular diameters to a precision of a few per cent, and to compete with intensity interferometry should a good flux calibration be achieved (Blackwell & Shallis 1977; Blackwell et al. 1979, 1980). Over the years, the IRFM has been successfully applied to determine effective temperatures in stars of different spectral types and metallicities (e.g., Alonso et al. 1996, 1999; Ramírez & Meléndez 2005; González Hernández & Bonifacio 2009; Casagrande et al. 2010).

The version of the IRFM used in this work has been previously validated against solar twins, HST absolute spectrophotometry and interferometric angular diameters (Casagrande et al. 2006, 2010). In particular, dedicated near-infrared photometry has been done to derive effective temperatures of interferometric targets with saturated 2MASS magnitudes (Casagrande et al. 2014). Our $T_{\rm eff}$ scale is widely used by many studies and surveys, and we now make it available into the Gaia photometric system. To do so, we implement Gaia photometry into the IRFM described in Casagrande et al. (2006, 2010). We run the IRFM for all stars in the Data Release 3 (DR3) of the GALAH survey (Buder et al. 2020), and provide colour$-T_{\rm eff}$ relations which take into account the effect of metallicity and surface gravity.

We describe how Gaia photometry is implemented into our version of the IRFM in Section 2 and present colour$-T_{\rm eff}$ relations in Section 3. We benchmark our results against standard stars, assess the typical $T_{\rm eff}$ uncertainty of our calibrations and provide guidelines for their use in Section 4. Finally, we draw our conclusions in Section 5.

2 THE INFRARED FLUX METHOD USING GAIA PHOTOMETRY

The IRFM can be viewed as the most extreme colour technique, relying on the index defined by the ratio between the bolometric and the infrared monochromatic flux of a star. This ratio can be compared to that obtained using the same quantities defined on a stellar surface element, $\sigma T_{\rm eff}^4$ and $\mathcal{F}_{\rm IR}$(model), respectively. If stellar and model fluxes are known, it is then possible to solve for $T_{\rm eff}$. As we describe later, this step is done iteratively in our version of the IRFM. The crucial advantage of the IRFM over other colour techniques is that, at least for spectral types hotter than early M-type, near-infrared photometry samples the Rayleigh–Jeans tail of stellar spectra, a region largely dominated by the continuum (but see Blackwell et al. 1991, for a discussion of the importance of H^- opacity), with a roughly linear dependence on $T_{\rm eff}$. The model dependent term $\mathcal{F}_{\rm IR}$(model) is very little affected by metallicity, sur-

⋆ Email:luca.casagrande@anu.edu.au

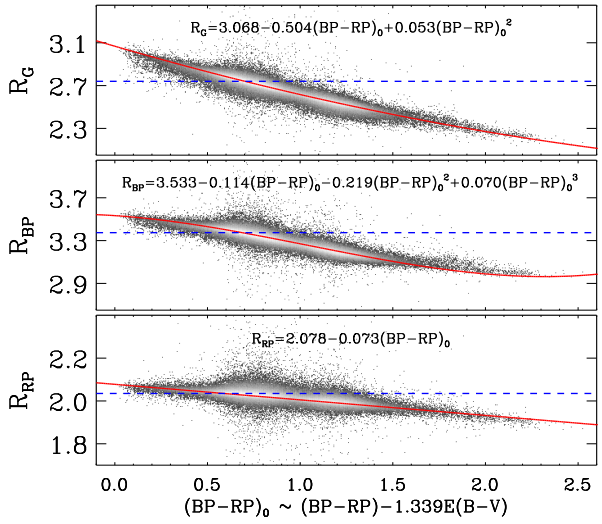

Figure 1. Gaia extinction coefficients as function of intrinsic stellar colours for our sample. Red solid lines show the fits given in each panel. Dotted blue lines are the average coefficients from Casagrande & VandenBerg 2018, which can be used to derive a first estimate of $(BP-RP)_0$ given $E(B-V)$.

face gravity and granulation as extensively tested in the literature (e.g., Alonso et al. 1996; Ramírez & Meléndez 2005; Casagrande et al. 2006; Casagrande 2009; González Hernández & Bonifacio 2009).

We use the implementation of the IRFM described in Casagrande et al. (2006, 2010), where for each star we now use Gaia BP, RP and 2MASS JHK_S photometry to derive the bolometric flux. The flux outside these bands (i.e., the bolometric correction) is estimated using a theoretical model flux at a given $T_{\rm eff}, \log(g)$ and [Fe/H]. The infrared monochromatic flux is derived from 2MASS magnitudes only. An iterative procedure in $T_{\rm eff}$ is adoped to cope with the mildly model-dependent nature of the bolometric correction and surface infrared monochromatic flux. For each star, we used the Castelli & Kurucz (2003) grid of model fluxes, starting with an initial estimate of its effective temperature and adopting the GALAH [Fe/H] and $\log(g)$, until convergence in $T_{\rm eff}$ is reached within 1K.

For Gaia BP and RP magnitudes we use the `Gaia-DR2` formalism described in Casagrande & VandenBerg (2018), which is based on the revised transmission curves and non-revised Vega zero-points provided by Evans et al. (2018). As described in Casagrande & VandenBerg (2018) this choice best mimics the photometric processing done by the Gaia team. We use BP and RP instead of G magnitudes for a number of reasons: comparison with absolute spectrophotometry indicates that BP and RP are reliable and well standardized in the magnitude range $\simeq 5$ to 16, which is relevant for our targets. On the contrary, G magnitudes have a magnitude dependent offset, and are affected by uncalibrated CCD saturation for $G \lesssim 6$ (Evans et al. 2018; Casagrande & VandenBerg 2018; Maíz Apellániz & Weiler 2018). Further, the BP and RP bandpasses together have the same wavelength coverage of the G bandpass.

One of the most critical points when implementing the IRFM is the photometric absolute calibration (i.e., how magnitudes are converted into fluxes), which sets the zero-point of the $T_{\rm eff}$ scale. This is particularly important in the infrared, for which we use the same 2MASS prescriptions discussed in Casagrande et al. (2010). To verify that the zero-point of our $T_{\rm eff}$ scale is not altered by Gaia magnitudes, we derive $T_{\rm eff}$ for all stars in Casagrande et al. (2010) with a counterpart in Gaia (408 targets). Not unexpectedly, we find excellent agreement, with a mean and median $\Delta T_{\rm eff} = 12 \pm 2$ K ($\sigma = 41$ K) and no trends as function of stellar parameters. This difference is robust, regardless of using stars with the best Gaia quality flags. Despite this difference is fully within the 20 K zero-point uncertainty of the reference $T_{\rm eff}$ scale of Casagrande et al. (2010), we correct for this small offset to adhere to the parent scale.

We apply the IRFM to over 620,000 stars in GALAH DR3 for which [Fe/H], $\log(g)$, BP, RP, J, H, K_S are available. About 40 percent of the targets have $E(B-V)$ from Green et al. (2019). For the remaining ones, we rescale reddening from Schlegel et al. (1998) with the same procedure described in Casagrande et al. (2019). To account for the spectral type dependence of extinction coefficients, in the IRFM we adopt the Cardelli et al. (1989)/O'Donnell (1994) extinction law, and for each star compute extinction coefficients with the synthetic spectrum at the $T_{\rm eff}, \log(g)$ and [Fe/H] used at each iteration.

The extinction coefficients we derive are in excellent agreement with the average ones reported in Casagrande & VandenBerg (2014) for JHK_S, and the $T_{\rm eff}$ dependent ones in G, BP and RP from Casagrande & VandenBerg (2018). For the purpose of the relations provided in this paper however, it is desirable to have an estimate of the extinction coefficients before the $T_{\rm eff}$ of a source is known. Figure 1 shows extinction coefficients for the Gaia filters as function of intrinsic (i.e. reddening corrected) stellar colour $(BP-RP)_0 = (BP-RP) - (R_{BP}-R_{RP})E(B-V)$.

The use of constant extinction coefficients instead of colour dependent ones affects colour indices, and hence the effective temperatures derived from the relations of Section 3. This can ben appreciated from the comparison in Figure 2, where the difference in colour obtained using constant or colour dependent extinction coefficients is amplified at high values of reddening for a given input $T_{\rm eff}$. The fits of Figure 1 should thus be preferred to deredden colour indices involvig Gaia bands, especially in regions of high extinction.

3 COLOUR–$T_{\rm eff}$ RELATIONS

In order to derive colour-effective temperature relations, we first apply a few quality cuts. We restrict ourselves to stars with best GALAH spectroscopic parameters (`flag_sp=0`), Gaia `phot_bp_rp_excess_factor` in the range $]1.0 + 0.015\,(BP-RP)^2, 1.3 + 0.060\,(BP-RP)^2[$ and `phot_proc_mode=0`. For relations involving the G band we also exclude a handful of stars with $G < 6$ (Evans et al. 2018; Riello et al. 2018). These requirements yield automatically good 2MASS photometry: median photometric errors in JHK_S are 0.024 mag with 99.9 percent of the targets having 2MASS quality flag `Qflg='AAA'`.

Depending on the combination of filters, there are over 360,000 stars available for out fits. Due to the combined effect of the GALAH selection function and target selection effects (most notably stellar evolutionary timescales), the distibution of targets has two main temperature overdensities: one at the main-sequence turn-off and the other at the red-clump phase. If all available stars were used to derive colour–$T_{\rm eff}$ relations these two overdensities would dominate the fit. Instead, we sample our stars uniformily in $T_{\rm eff}$, randomly selecting 20 stars every 20 K, and repeating this for 10 realizations. The calibration sample for each fit is thus based on roughly 50,000 stars. We repeat the above procedure 10,000 times, and select the fit that returns the lowest standard deviation with re-

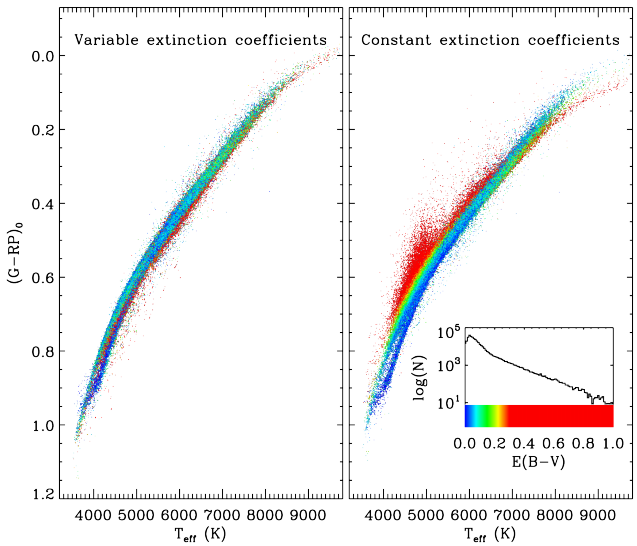

Figure 2. Left panel: colour-$T_{\rm eff}$ relation obtained from the IRFM in $(G-RP)_0$, where extinction coefficients are computed for each star individually. Right panel: colour-$T_{\rm eff}$ relation using the same input effective temperatures, but constant extinction coefficients to deredden the colour index. The importance of using variable extinction coefficients becomes visible for increasing values of reddening. Stars are colour coded by their $E(B-V)$ with the distribution shown in the inset.

spect to the input effective temperatures from the IRFM. We also explored the effect of a uniform gridding in $T_{\rm eff}$ and $\log(g)$ but did not find any significant difference with respect to a uniform sampling in $T_{\rm eff}$ only.

To derive our relations we started with a polynomial as function of colour, which is the parameter that has the strongest dependence on $T_{\rm eff}$. Depending on the colour index, we found that a third or fifth order polynomial was necessary to describe the curve inflection occurring at low $T_{\rm eff}$. We then added the [Fe/H] and $\log(g)$ dependence into the fit. The Gaia broad band filters have a rather mild dependence on metallicity, and the effect of $\log(g)$ is most noticeable below 4500 K, where colour-$T_{\rm eff}$ relations for dwarf and giant stars branch off (Figure 3 and 4). We found no need to go higher than first order in [Fe/H] and $\log(g)$, but cross-terms with colour, as well as a term involving colour, $T_{\rm eff}$ and $\log(g)$ were found to ameliorate the fit. The adopted functional form is:

$$T_{\rm eff} = a_0 + a_1 X + a_2 X^2 + a_3 X^3 + a_4 X^5 + a_5 \log(g) + a_6 \log(g)\, X + a_7 \log(g)\, X^2 + a_8 \log(g)\, X^3 + a_9 \log(g)\, X^5 + a_{10}[\mathrm{Fe/H}] + a_{11}[\mathrm{Fe/H}]\, X + a_{12}[\mathrm{Fe/H}]\, X^2 + a_{13}[\mathrm{Fe/H}]\, X^3 + a_{14}[\mathrm{Fe/H}] \log(g)\, X \quad (1)$$

where X is the colour index corrected for reddening, and not all terms were found to be significant for all colour indices. The coefficients of Eq. 1 are given in Table 1.

Figure 3 shows the colour-$T_{\rm eff}$ relation for $(BP-RP)_0$, along with the residuals of the fit as function of colour, gravity and metallicity. Although Eq. (1) virtually allows for any combination of input parameters, it should be recalled that stars distribute across the HR diagram as permitted by stellar evolutionary theory. Figure 4a illustrates the range of stars used to build our colour calibrations, where cool stars are found both at low and high surface gravities, whereas the hottest stars have $\log(g) \sim 4$. Fig 4b and 4c show the dependence on $\log(g)$ and [Fe/H] for some of ours color-$T_{\rm eff}$ calibrations. Plotted for comparison are also predictions from synthetic stellar fluxes computed with the `bolometric-corrections`[1] code (Casagrande & VandenBerg 2014, 2018). The purpose of this comparison is not to validate empirical nor theoretical relations, but to show that our functional form well captures the expected change of colours with $T_{\rm eff}$, $\log(g)$ and [Fe/H]. Some of the discrepancies between empirical and theoretical predictions at the coolest $T_{\rm eff}$ are likely due to inadequancies of synthetic fluxes as discussed in the literature (see e.g., Casagrande & VandenBerg 2014; Böcek Topcu et al. 2020)

4 VALIDATION AND UNCERTAINTIES

We validate our colour-$T_{\rm eff}$ relations using three different approaches: solar twins, Gaia benchmark stars and interferometric measurements. The stars used for this purpose are some of the brightest and best observed in the sky, with careful determinations of their stellar parameters. In all instances, we apply the same requirements on `phot_bp_rp_excess_factor` and `phot_proc_mode` discussed in Section 3 to select best photometry. We also exclude $G < 6$ and BP and $RP < 5$ due to uncalibrated systematics at bright magnitudes. We only use 2MASS photometry with `'A' Qflg` in a given band.

The sample of solar twins is the same used in Casagrande et al. (2010) to set the zero-point of their $T_{\rm eff}$ scale. These twins are all nearby, unaffected by reddening and with good Gaia and 2MASS photometry. Accurate and precise spectroscopic $T_{\rm eff}$, $\log(g)$ and [Fe/H] are available from differential analysis of high-resolution, high S/N spectra with respect to a solar reference one (Meléndez et al. 2009). In Table 2 we report the mean difference between the effective temperatures we derive in a given colour index, and the spectroscopic ones. Our $T_{\rm eff}$ are typically within few degrees of the spectroscopic ones. Further, regardless of the spectroscopic effective temperatures, the mean and median $T_{\rm eff}$ for our sample of solar twins in any colour index is always within few tens of K of the solar $T_{\rm eff}$. The fact that our colour-$T_{\rm eff}$ relations are well calibrated around the solar value is not unexpected, but confirms that we have achieved our goal of tying the current $T_{\rm eff}$ scale to that of Casagrande et al. (2010).

For the Gaia Benchmark Stars (GBS) we use $T_{\rm eff}$, $\log(g)$ and [Fe/H] from the latest version of the catalog (Jofré et al. 2018). The number of stars with good photometry varies depending on the filter used. All GBS in our sample are closer than $\simeq$ 130 pc, justifying the adoption of zero reddening. Again, we find overall excellent agreement between the $T_{\rm eff}$ we predict from colours, and those given in the GBS catalog.

Finally, we assemble a list of interferometric measurements from the recent literature: Bigot et al. (2011), Boyajian et al. (2012), Huber et al. (2012), Maestro et al. (2013), White et al. (2013, 2018), Gallenne et al. (2018), Rains et al. (2020) and Karovicova et al. (2020). For all these stars we adopt reddening, $\log(g)$ and [Fe/H] reported in the above papers. This list encompasses over 110 targets, although most of them are very bright, hence with unreliable Gaia and/or 2MASS magnitudes, reducing the sample usable for our comparison to maximum 30 targets depending on the colour index. For the comparison in Table 2 we further require interferometric $T_{\rm eff}$ to be better than 1 percent, which is the target accuracy we aim at testing. Allowing for larger uncertainties results in an

[1] https://github.com/casaluca/bolometric-corrections

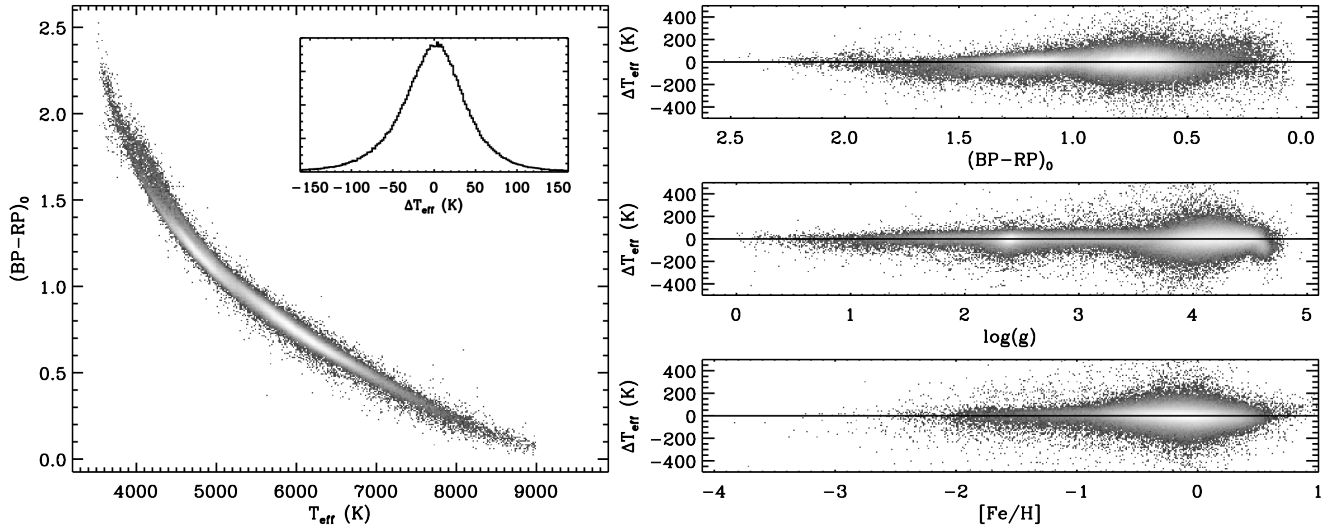

Figure 3. Left panel: density plot of the colour-$T_{\rm eff}$ relation obtained using all 360,000 GALAH stars with good photometric and spectroscopic flags as described in the text. For $T_{\rm eff} \lesssim 4500$ K the two loci defined by dwarf and giant stars can be clearly noticed. The inset shows the distribution of the $T_{\rm eff}$ residuals of our calibration. Right panels: $T_{\rm eff}$ residuals plotted as function of colour, surface gravity and metallicity. Plots for the other colour indices are available as supplementary online material.

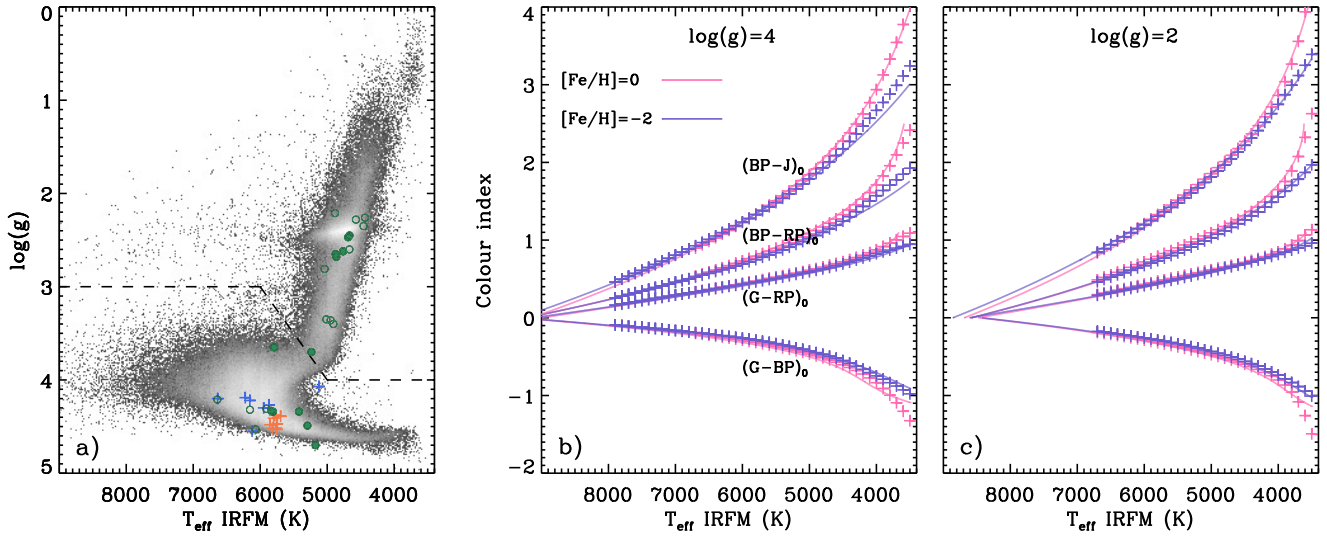

Figure 4. Left panel: Kiel diagram of the GALAH sample used to derive the colour-$T_{\rm eff}$ relations presented in this work. The dashed line marks the separation between dwarf and giant stars discussed in Section 4. Coloured crossed and circles are the stars used in Fig 5 to test the $T_{\rm eff}$ scale. Middle and right panels: some of the colour-$T_{\rm eff}$ relations (solid lines) of Table 1 for fixed values of $\log(g) = 4$ and $\log(g) = 2$, and [Fe/H] = 0 and [Fe/H] = −2, as labelled. Plotted for comparison are synthetic colour-$T_{\rm eff}$ computed for the same values of gravity and metallicity (cross symbols). Note that the maximum $T_{\rm eff}$ available for synthetic colours varies with the adopted $\log(g)$.

increase of scatter in the comparison, with a trend whereby interferometric $T_{\rm eff}$ are systematically cooler for stars with the largest uncertainties. This is indicative that systematic errors tend to over-resolve angular diameters, hence under-predict effective temperatures (see discussion in Casagrande et al. 2014).

Overall, it is clear from Table 2 that our relations are able to predict $T_{\rm eff}$ in very good agreement with those reported in the literature for various benchmark samples. Depending on the colour index, mean differences are typically of order few tens of K. Occasional larger differences are still within the scatter of the relations, or likely due to low number statistic. When restricting to the $(BP - RP)_0$ colour index, which has the largest number of stars available for comparison, the mean agreement is always within a few K regardless of the sample used (Figure 5).

From a user point of view, it is important to have realistic estimates of the precision at which $T_{\rm eff}$ can be estimated from our relations. In Table 1 we report two values for the standard deviation of our color-$T_{\rm eff}$ relations. The first value is the precision of the fits. The second one provides a more realistic assessment of the uncertainties encountered when applying our relations, and it is obtained by randomly perturbing the input [Fe/H] and $\log(g)$ with a Gaussian distribution of width 0.2 and 0.5 dex, respectively. It should be kept

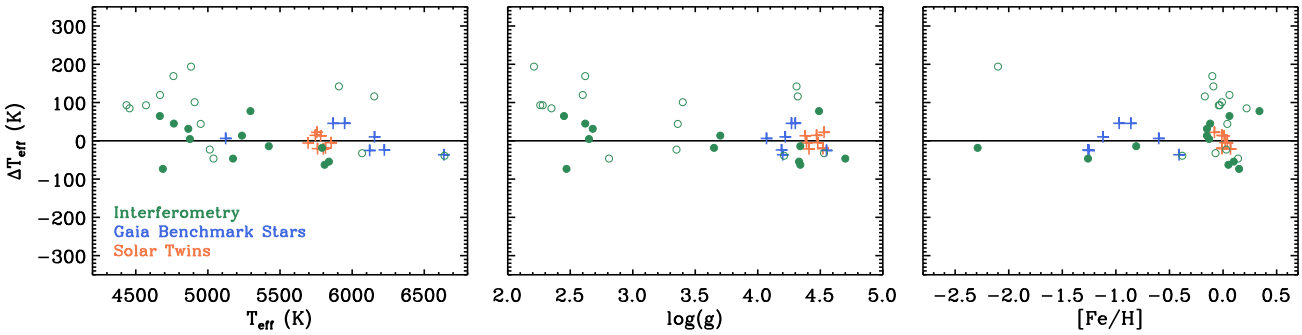

Figure 5. Comparison between $T_{\rm eff}$ derived using our $(BP-RP)_0$ relation and those available from the literatures for solar twins (orange), Gaia Benchmark Stars (blue) and interferometry (green). Filled and open circles indicate interferometric $T_{\rm eff}$ better than 1 and 2 percent, respectively.

Table 2. Mean difference and standard deviation between the effective temperatures derived from our calibrations, and those from the literature used for validation (ours−literature). N is the number of stars available in each colour index.

colour	Solar Twins		GBS		Interferometry†	
	$\langle\Delta T_{\rm eff}\rangle$	N	$\langle\Delta T_{\rm eff}\rangle$	N	$\langle\Delta T_{\rm eff}\rangle$	N
$(BP-RP)_0$	-3 ± 17	8	3 ± 34	7	-3 ± 51	12
$(BP-J)_0$	-6 ± 23	8	10 ± 55	5	9 ± 48	3
$(BP-H)_0$	10 ± 13	8	49 ± 48	5	95 ± 8	2
$(BP-K)_0$	-14 ± 21	8	-16 ± 32	6	-30 ± 60	6
$(RP-J)_0$	-13 ± 69	8	2 ± 108	5	-42 ± 112	3
$(RP-H)_0$	-2 ± 36	8	25 ± 74	5	68 ± 14	2
$(RP-K)_0$	-28 ± 37	8	-52 ± 40	6	-51 ± 59	6
$(G-J)_0$	-2 ± 36	8	-4 ± 72	5	-16 ± 49	3
$(G-H)_0$	5 ± 20	8	18 ± 59	5	60 ± 50	2
$(G-K)_0$	-27 ± 26	8	-52 ± 40	5	-54 ± 74	5
$(G-BP)_0$	-30 ± 16	8	-19 ± 42	5	-38 ± 59	5
$(G-RP)_0$	0 ± 22	8	10 ± 31	5	-17 ± 66	5

†Only interferometric $T_{\rm eff}$ better than 1 percent are used.

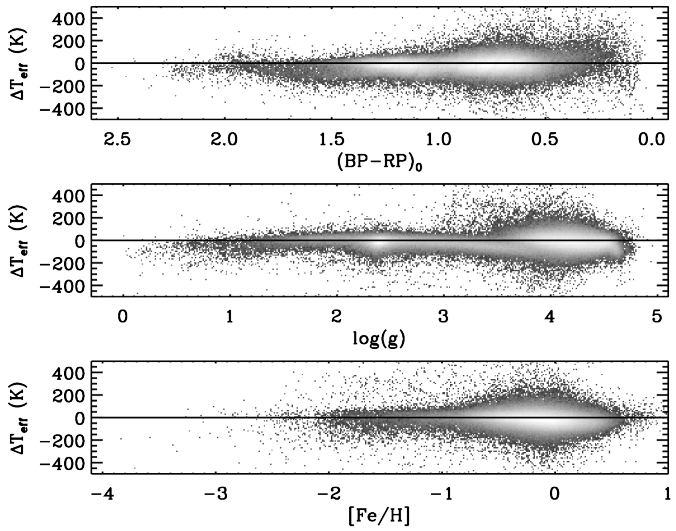

Figure 6. $T_{\rm eff}$ residual for the $(BP-RP)_0$ calibration when stars are assigned a fixed $\log(g)=2$ or 4 based on their classification as giants or dwarfs as per Figure 4. Plots for the other colour indices are available as supplementary online material.

in mind that uncertainties in input stellar parameters will propagate differently with different colours, the effect being strongest for the coolest stars. Users of our calibrations are encouraged to assess their uncertainties on a case-by-case basis, by propagating in Eq. 1 errors in their input parameters. Further, an extra uncertainty of 20 K should still be added to account for the zero-point uncertainty of our $T_{\rm eff}$ scale.

Although our calibrations take into account the effect of surface gravity, there might be instances where the input $\log(g)$ is not known, besides a rough "dwarf" vs "giant" classification. To assess this impact, we classify stars as dwarfs (giants) if their gravities are higher (lower) than the dashed line of Figure 4a. We then adopt a constant $\log(g)=4$ for dwarfs and $\log(g)=2$ for giants. The effect of such assumption on the derived $T_{\rm eff}$ is typically small, as it can be appreciated from Figure 6. The largest differences occur for stars in the upper giant branch, where assuming a constant $\log(g)=2$ become inappropriate below $\simeq 1-1.5$. This effect can be quite strong on certain colour indices. In this case, one might use the fact that there is a strong correlation between the intrinsic colour and the surface gravity of stars along the RGB for a better assignment of $\log(g)$.

5 CONCLUSIONS

In this paper we have implemented the Gaia photometric system in the IRFM and used it to derive $T_{\rm eff}$ for stars across different evolutionary phases. In the literature, colour-$T_{\rm eff}$ relations for late type-stars are typically given separately for dwarfs and giants. The advent of Gaia parallaxes allows us to use robust surface gravities together with [Fe/H] from the GALAH DR3 survey to provide colour-$T_{\rm eff}$ relations that take into account the effect of these two parameters over the range $\simeq$ 3600 – 9000 K. Our calibrations are built using the largest high-resolution stellar spectroscopic survey to date and cover a wide range of stellar colours and parameters: $0\lesssim\log(g)\lesssim4.5$ and $-3\lesssim$[Fe/H]$\lesssim0.6$. As such, a simple colour range for the applicability of our relations is of little use, since stars do not fill this parameter space uniformly. Users should refer to Figures 3 and 4 to have a sense for the space parameter covered when using our relations. For $T_{\rm eff}<6700$ K our calibrations are validated against solar twins, Gaia benchmark stars and interferometry.

Table 1. Coefficients and range of applicability of the $T_{\rm eff}$ calibration of Eq. 1.

colour	a_0	a_1	a_2	a_3	a_4	a_5	a_6	a_7	a_8	a_9	a_{10}	a_{11}	a_{12}	a_{13}	a_{14}	$\sigma(T_{\rm eff})$ (K)
$(BP-RP)_0$	7928	−3663.1140	803.3017	−9.3727	–	325.1324	−500.1160	279.4832	−53.5062	–	−2.4205	−128.0354	49.4933	5.9146	41.3650	54 – 66
$(BP-J)_0$	8218	−2526.8430	458.1827	−28.4540	–	234.0113	−205.3084	63.4781	−7.2083	–	−85.7048	−50.1557	32.3428	−2.3553	20.0671	44 – 49
$(BP-H)_0$	8462	−2570.3684	537.5968	−44.3644	–	189.1198	−106.7584	31.1720	−4.9137	–	−9.2587	−189.8600	75.8619	−6.8592	16.7226	33 – 42
$(BP-K)_0$	8404	−2265.1355	403.4693	−27.9056	–	193.5820	−145.3724	47.7998	−6.4572	–	−34.5438	−130.2559	52.6470	−4.4777	15.8249	24 – 32
$(RP-J)_0$	9074	−7670.6606	3164.0525	–	−126.1476	–	−7.3816	−12.5168	–	−2.0452	–	76.1144	–	–	−45.8056	90 – 95
$(RP-H)_0$	8924	−4779.3394	1319.8989	–	−16.6676	–	−23.6583	22.4243	–	−4.3066	–	35.0102	–	–	−28.7222	52 – 62
$(RP-K)_0$	8940	−4450.6138	1138.6816	–	−10.5749	–	−42.3037	33.3365	–	−3.2535	–	41.0402	–	–	−21.9922	43 – 48
$(G-J)_0$	8370	−3559.7710	895.8869	−86.7011	–	180.7568	−164.9264	24.4263	4.2318	–	−127.9640	72.1449	–	–	13.7683	54 – 57
$(G-H)_0$	8186	−2536.7671	503.2762	−42.7871	–	230.4871	−254.5291	104.6258	−17.4859	–	−122.0732	45.0572	–	–	6.9992	37 – 41
$(G-K)_0$	8103	−1857.7194	–	73.1834	−1.7576	236.0335	−345.9070	170.4915	−28.8549	–	−131.4548	49.6232	–	–	10.0777	27 – 32
$(G-BP)_0$	7555	5803.7715	–	−2441.7124	437.7314	455.0997	2243.1333	3669.4924	1872.7035	–	19.1085	75.2198	–	–	−83.9777	75 – 93
$(G-RP)_0$	7971	−5737.5049	–	1619.9946	−203.8234	255.7408	−492.8268	160.1957	103.1114	–	−64.3289	34.3339	–	–	54.7224	56 – 64

G magnitudes have been corrected following Maíz Apellániz & Weiler (2018): $G + 0.0271\,(6-G)$ for $G \leqslant 6$, $G - 0.0032\,(G-6)$ for $6 < G < 16$ and $G - 0.032$ for $G \geqslant 16$. Users should be wary of applying these relations to stars with $G < 6$ and BP and RP brighter than ~ 5 due to the saturation of bright magnitudes in Gaia. For the standard deviation of the calibration $\sigma(T_{\rm eff})$, we provide two estimates, both obtained using all available $\sim 360,000$ stars, instead of the $\sim 50,000$ used to derive fits. The first one is the precision of the fits, whereas for the second one input [Fe/H] and $\log(g)$ are perturbed with a Gaussian random noise of 0.2 and 0.5 dex, respectively. Note that an extra uncertainty of about 20 K on the zero-point of our effective temperature scale should still be added.

ACKNOWLEDGMENTS

LC is the recipient of an ARC Future Fellowship (project number FT160100402). Parts of this research were conducted by the Australian Research Council Centre of Excellence for All Sky Astrophysics in 3 Dimensions (ASTRO 3D), through project number CE170100013. This work has made use of data from the European Space Agency (ESA) mission *Gaia* (`https://www.cosmos.esa.int/gaia`), processed by the *Gaia* Data Processing and Analysis Consortium (DPAC, `https://www.cosmos.esa.int/web/gaia/dpac/consortium`). Funding for the DPAC has been provided by national institutions, in particular the institutions participating in the *Gaia* Multilateral Agreement.

REFERENCES

Alonso A., Arribas S., Martinez-Roger C., 1996, A&A, 313, 873
Alonso A., Arribas S., Martínez-Roger C., 1999, A&AS, 140, 261
Bigot L. et al., 2011, A&A, 534, L3
Blackwell D. E., Shallis M. J., 1977, MNRAS, 180, 177
Blackwell D. E., Shallis M. J., Selby M. J., 1979, MNRAS, 188, 847
Blackwell D. E., Petford A. D., Shallis M. J., 1980, A&A, 82, 249
Blackwell D. E., Lynas-Gray A. E., Petford A. D., 1991, A&A, 245, 567
Böcek Topcu G. et al., 2020, MNRAS, 491, 544
Boyajian T. S. et al., 2012, ApJ, 746, 101
Buder S. et al., 2020, MNRAS submitted
Cardelli J. A., Clayton G. C., Mathis J. S., 1989, ApJ, 345, 245
Casagrande L., 2009, Mem. Soc. Astron. Italiana, 80, 727
Casagrande L., VandenBerg D. A., 2014, MNRAS, 444, 392
Casagrande L., VandenBerg D. A., 2018, MNRAS, 479, L102
Casagrande L., Portinari L., Flynn C., 2006, MNRAS, 373, 13
Casagrande L., Ramírez I., Meléndez J., Bessell M., Asplund M., 2010, A&A, 512, A54
Casagrande L., Wolf C., Mackey A. D., Nordland er T., Yong D., Bessell M., 2019, MNRAS, 482, 2770
Casagrande L. et al., 2014, MNRAS, 439, 2060
Castelli F., Kurucz R. L., 2003, in N. Piskunov, W.W. Weiss, D.F. Gray, eds, Modelling of Stellar Atmospheres. IAU Symposium, Vol. 210, p. A20
Choi J., Dotter A., Conroy C., Ting Y. S., 2018, ApJ, 860, 131
Code A. D., Bless R. C., Davis J., Brown R. H., 1976, ApJ, 203, 417
Evans D. W. et al., 2018, A&A, 616, A4
Gallenne A. et al., 2018, A&A, 616, A68
González Hernández J. I., Bonifacio P., 2009, A&A, 497, 497
Green G. M., Schlafly E., Zucker C., Speagle J. S., Finkbeiner D., 2019, ApJ, 887, 93
Huber D. et al., 2012, ApJ, 760, 32
Jofré P., Heiter U., Tucci Maia M., Soubiran C., Worley C. C., Hawkins K., Blanco-Cuaresma S., Rodrigo C., 2018, Research Notes of the American Astronomical Society, 2, 152
Karovicova I., White T. R., Nordlander T., Casagrand e L., Ireland M., Huber D., Jofré P., 2020, A&A, 640, A25
Lachaume R., Rabus M., Jordán A., Brahm R., Boyajian T., von Braun K., Berger J. P., 2019, MNRAS, 484, 2656
Maestro V. et al., 2013, MNRAS, 434, 1321
Maíz Apellániz J., Weiler M., 2018, A&A, 619, A180
Meléndez J., Asplund M., Gustafsson B., Yong D., 2009, ApJ, 704, L66
Nissen P. E., Gustafsson B., 2018, A&A Rev., 26, 6
O'Donnell J. E., 1994, ApJ, 422, 158
Rains A. D., Ireland M. J., White T. R., Casagrande L., Karovicova I., 2020, MNRAS, 493, 2377
Ramírez I., Meléndez J., 2005, ApJ, 626, 465
Riello M. et al., 2018, A&A, 616, A3
Schlegel D. J., Finkbeiner D. P., Davis M., 1998, ApJ, 500, 525
White T. R. et al., 2013, MNRAS, 433, 1262
White T. R. et al., 2018, MNRAS, 477, 4403